ADVANCED FUNCTIONAL MATERIALS
www.afm-journal.de

Bidirectionally High-Thermally Conductive and Environmentally Adaptive Graphene Thick Films Enabled by Seamless Bonding Assembly for Extreme Thermal Management

Yuanyuan Hao, Xin Ming, Jiahao Lu, Min Cao, Peijuan Zhang, Hang Shi, Kaiwen Li, Yue Gao, Lidan Wang, Wenzhang Fang, Yance Chen, Lin Zhang, Haiyan Sun, Weiwei Gao, Yingjun Liu, Zhen Xu,* and Chao Gao**

With the rapid development of high-power electronics in aerospace, communication, and energy storage systems, the huge heat flux poses an increasing threat to the safety of electronic devices. Compared with thin films of a few micro thicknesses, high-quality graphene thick film (GTF) exceeding hundreds of microns thickness is a promising candidate to solve thermal management challenges owing to higher heat-flux. However, traditional GTF usually has lower thermal conductivity and weak mechanical properties attributed to disordered sheet alignment and frail interfacial adhesion. Here, a seamless bonding assembly (SBA) strategy is proposed to attain GTF over record hundreds of microns with robust coalescence interfaces. For the GTF-SBA with ≈250 µm thickness, the in-plane and through-plane thermal conductivities are 925.75 and 7.03 W m^{-1} K^{-1}, approximately two times and 12 times those of the GTF prepared by traditional adhesive assembly method, respectively. Furthermore, the GTF-SBA demonstrates remarkable stability even after cycled harsh temperature shocks from 77 to 573 K, ensuring its environmental adaptability for long-term service in extreme conditions. These findings provide valuable insights into the interfacial design of graphene bulk materials and highlight the potential applications of high-performance graphene-based materials for extreme thermal management demands.

1. Introduction

The rapid development of high-power electronics in the aerospace field has required greater integration and miniaturization,[1–3] which inevitably generates localized high heat flux during operation.[4–7] In extreme service environments, such as alternating temperatures in outer space, there is a risk of thermal management modules facing catastrophic structural failures.[8–12] Developing novel thermal management materials is crucial to exploring the next generation of aerospace thermal control technology to meet the demanding requirements of lightweight, high thermal conductivity, and exceptional structural stability, particularly in extreme application conditions.[13–15] Large-area graphene film (GF) inherits the superb thermal conductivity of original 2D graphene sheets as a promising carbon-based thermal management material in widespread aerospace and electronics applications,[16–27] which

Y. Hao, X. Ming, J. Lu, M. Cao, P. Zhang, H. Shi, K. Li, Y. Gao, L. Wang, W. Fang, Y. Chen, L. Zhang, W. Gao, Y. Liu, Z. Xu, C. Gao
MOE Key Laboratory of Macromolecular Synthesis and Functionalization
Department of Polymer Science and Engineering
Key Laboratory of Adsorption and Separation Materials & Technologies of Zhejiang Province
Zhejiang University
38 Zheda Road, Hangzhou 310027, China
E-mail: yingjunliu@zju.edu.cn; zhenxu@zju.edu.cn; chaogao@zju.edu.cn

H. Sun
Hangzhou Gaoxi Technology Co Ltd
Hangzhou 311113, China

W. Gao, Y. Liu, Z. Xu, C. Gao
Shanxi-Zheda Institute of Advanced Materials and Chemical Engineering
Taiyuan China

The ORCID identification number(s) for the author(s) of this article can be found under https://doi.org/10.1002/adfm.202400110

DOI: 10.1002/adfm.202400110

could be obtained through various bottom-up macro-assembly methods such as blade coating,[28] filtration,[29] wet spinning,[30] and centrifugal casting.[31] However, it remains challenging for GF to deliver robust thermal management performance to handle the high heat flux levels (1000 W cm^{-2}) experienced in extreme environments,[32] partly arising from the tradeoff between the desired thermal conductivity and maintaining the thicker film thickness.[33,34] In addition, it is more essential to consider the structural stability of GF to ensure their long-term and reliable performance in diverse practical applications.

Until now, the thickness of reported conventional GF through the bottom-up assembly of graphene oxide (GO) is typically less than 50 µm,[35–37] resulting in unsatisfied practical heat dissipation capabilities. Furthermore, fabricating the hundred-micron graphene thick film (GTF) with excellent thermal transfer capacity is constrained by the assembly technology required for creating nonporous and stable interface structures in typical layered materials.[38–40] Generally, the assembly route of GTF could be divided into two main trends, including direct assembling of GO-based slurry through blade coating[41] or filtration[42] and indirect assembling of multiple individual GO-based or GF units.[43,44] Due to the inevitable skin effect during the time-consuming GO slurry drying process,[45] neither increasing the concentration nor volume of the GO slurry to increase film thickness could avoid the formation of chaotic orientation of graphene sheets and numerous pores in the final GTF after heat treatments,[41,42] which drastically diminish the thermal conductivity with lower heat flux. Besides, the GTF obtained through indirect methods, such as swelling bonding of GO films based on the self-fusion character,[43] stacking of GO-based films by the mechanical pressing,[44] and welding of GF by Joule heating,[46] often suffer from weak interfacial adhesion and uncontrollable process, resulting in non-dense structures. Presently, commercial GTF is manufactured by stacking and adhering separated GF (<50 µm) through the traditional adhesive assembly (TAA) roadmap. While the TAA is efficient and convenient, it presents inherent limitations, including air gaps at the interfaces, the low thermal conductivity of polymer adhesives,[47] and structural instability in extreme conditions due to polymer embrittlement at low temperatures and decomposition at high temperatures.[48] It is worth noting that the acquired GTF through the aforementioned assembly methods is almost neat graphene material with low through-plane thermal conductivity ($\kappa_{\perp}$) limiting the overall heat transfer.[49] Additionally, in extreme scenarios, such as liquid nitrogen, GTF is prone to bubbling and stratification failure due to the inner defects within the GF. Therefore, fabricating GTF over a hundred-micron thickness with high thermal conductivity in both directions and extreme environmental tolerance remains a great challenge.

Here we introduce a seamless bonding assembly (SBA) strategy to fabricate hundred-micron-thickness GTF, exhibiting impressive bidirectionally high thermal conductivity and exceptionally stable structure. It is realized through a modular design of GF matrix units and ultra-thin ternary seamless bonding interfaces. The seamless bonding nanolayers consist of ternary Ag/Cu/Ti composite to ensure the reliable integration of GF units. The resultant GTF-SBA with ≈250 µm thickness possesses a high in-plane thermal conductivity ($\kappa_{\parallel}$) of 925.75 W m^{-1} K^{-1} and the highest $\kappa_{\perp}$ of 7.03 W m^{-1} K^{-1} among all reported GTF. Moreover, the SBA engineering ensures that the GTF achieves exceptional environmental adaptability in multiple harsh temperature shocks from 77 to 573 K, which underscores the suitability of GTF-SBA for extreme thermal management. Our study provides a solid way to endow GTF with bidirectionally high thermal conductivity and reliable structural stability, triggering a rational interfacial design principle for extreme thermal management.

2. Result and Discussion

2.1. Seamless Bonding Assembly Strategy for GTF

Commercially available GTF is typically prepared by the TAA method. Several thin GFs are overlapped and adhered together via polyacrylate-based adhesives, followed by cold-pressed (Figure 1a; Figure S1, Supporting Information). However, the physical adhesion-dominated assembly encounters significant challenges in terms of thermal conductivity degradation and structural instability when exposed to extreme conditions. These issues mainly arise from the chemically inert surface of GF and interfacial incompatibility of polymer, which induce non-negligible unstable and porous interfaces.

To achieve high thermal conductivity and ultra-stability of GTF, we propose a reliable SBA process to effectively eliminate interfacial porosity and enhance interfacial bonding. The designed SBA route involves a multi-step ionic implantation, metal magnetron sputtering, and spark plasma sintering process to construct a seamless and robust interface of GTF-SBA (Figure 1a). Specifically, a trace amount of Ti is introduced to boost the surface reactivity of GF units through ionic implantation, which lays the foundation of seamlessly metalized interfaces. Then, the sequential magnetron sputtering deposition of Cu (≈250 nm) and Ag (≈250 nm) nanolayers on the surface of Ti-modified GF to realize the metalized GF (MGF) (Figure S2, Supporting Information). Finally, the individual MGF is seamlessly assembled through spark plasma sintering to realize the coalescence of metallic layers to fabricate GTF-SBA (Figures S3–S5, Supporting Information). The rationally designed interfacial constituents and microstructures of GTF-SBA ultimately lead to solidly seamless bonding for outstanding thermal management performance.

As shown in Figure 1b, the cross-section of GTF-TAA possesses numerous voids, which originated from the non-conformable adhesion of polymer on the subtle surface wrinkles of GF. These undesired voids are filled with low thermal conductive air, seriously increasing the interfacial thermal resistance and becoming the root cause of structure failure under extreme conditions. Guided by the seamless assembly concept, the GTF-SBA exhibits a tight, dense, and continuous interfacial layer with dramatically eliminating interface defects, in which interfacial porosity is reduced to 1/6 of GTF-TAA (Figure 1c,d). It is particularly noteworthy that the GTF-SBA could be easily assembled into controllable thickness, size, and shape attributed to the high efficiency and scalable compatibility of SBA, which provides a new technical solution for the demanding of irregular thermal management components (Figure 1e,f; Figure S6 and Table S1, Supporting Information). Therefore, the GTF-SBA shows a substantial improvement in the interfacial structure compactness and overall thermal conductive performance in full-temperature

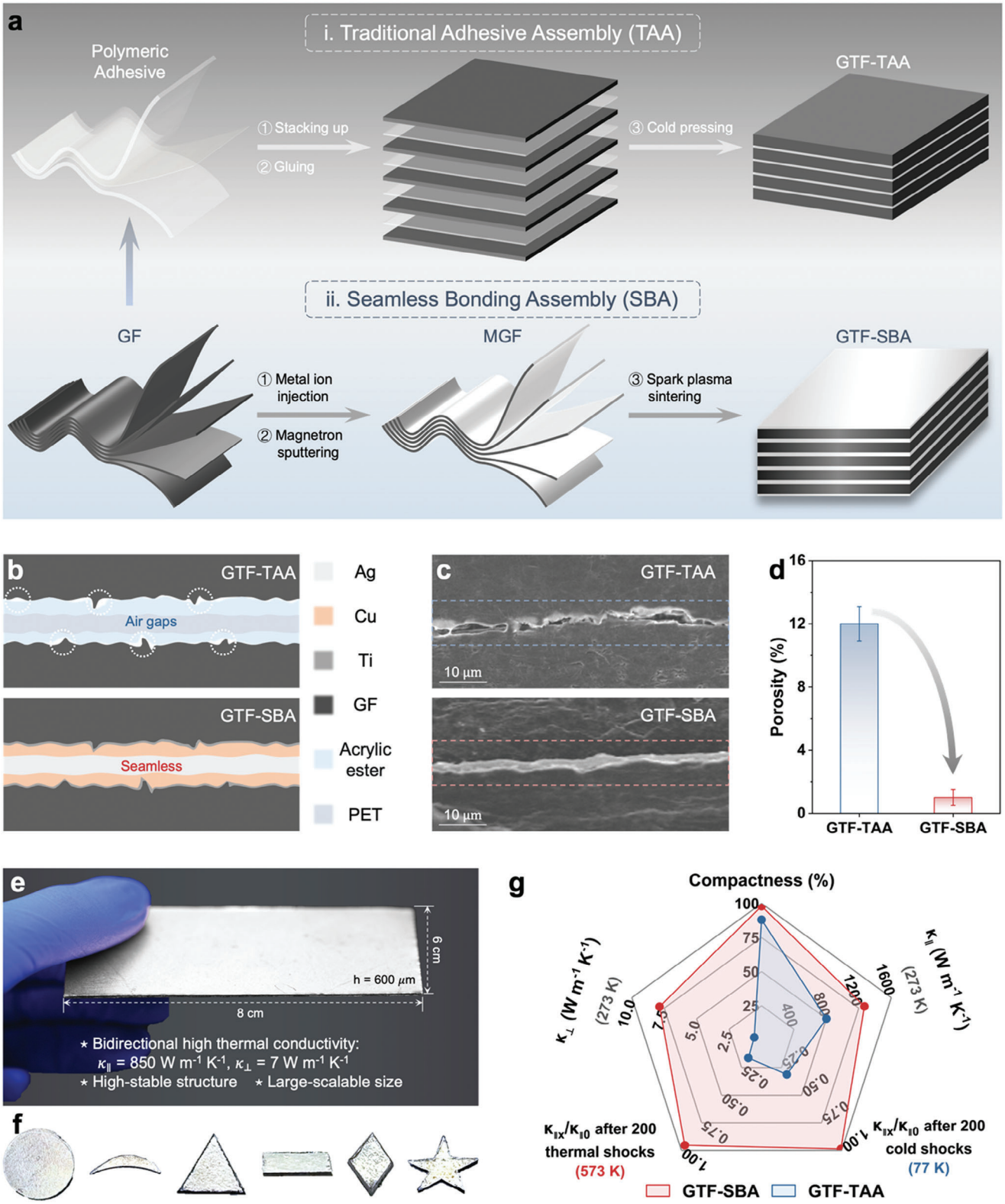

Figure 1. a) Schematic of the scalable fabrication process of the GTF-TAA and GTF-SBA. b) Illustration of the bonding interfaces of the GTF-TAA and GTF-SBA with different interfacial microporous structures. c) SEM images of the bonding interfaces of the GTF-TAA and GTF-SBA. d) Interfacial porosity of the GTF-TAA and GTF-SBA. e) Optical images of the large-scale GTF-SBA bulk material. f) Optical images of the GTF-SBA with controllable shapes and thicknesses. g) The interface compactness and overall thermal conductive performances of GTF-SBA (red line) and GTF-TAA (blue line). The thicknesses of GTF-TAA and GTF-SBA are ≈100 microns.

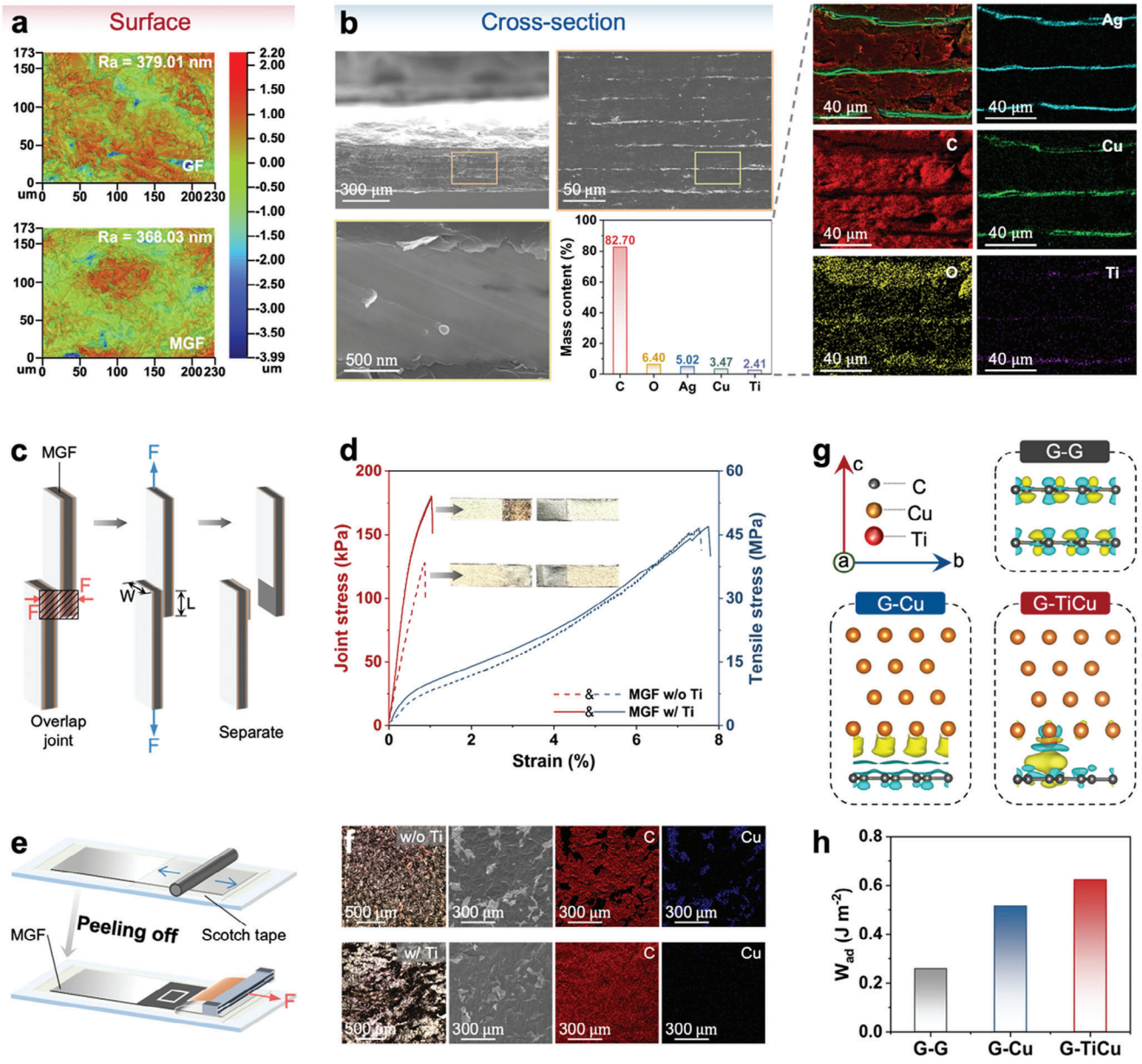

Figure 2. a) Surface roughness of GF and MGF. b) SEM images of GTF and corresponding elemental mapping images of C, O, Ag, Cu, and Ti. c) Schematic of the lap shear measurement. d) Joint stress-strain curves and tensile stress-strain of the MGF without Ti and with Ti. The insets are optical images of the MGF after a shear failure. e) Schematic of the peeling test of the metal deposition layer on the MGF. f) Optical images and SEM images of the MGF peeled off by 3 M scotch tape (the part circled by the white frame). g) DFT calculations of differential charge density distribution of graphene/graphene, graphene/Cu, and graphene/TiCu interfaces. h) Adhesion work of three interfacial structures. Yellow electron cloud shows the accumulation of charge and blue shows the consumption of charge.

zones, which supports the reliable extreme thermal management materials (Figure 1g).

2.2. Design and Characterization of Seamlessly Ultrathin Metalized Interfaces

The interfacial composition and microstructure of the seamlessly ultrathin metalized interfaces build the foundation for seamless and tight assembly, which makes GTF-SBA possess outstanding thermal conductivity and environmental adaption. The surface roughness of the MGF (Ra = 368.03 nm) is slightly lower than the origin GF (Ra = 379.01 nm), which originates from the continuously smooth metal nanolayers (Figure 2a; Figure S7 and S8, Supporting Information). It indicates that the ultrathin metalized bonding interface is extremely conformable with the GF assembly units for reduced interfacial porosity. Furthermore, the slightly increased microscopic flatness of the MGF also benefits for subsequent seamless assembly. The GTF-SBA shows closely stacked lamellar and seamless bonding structures with

sequentially existing Ag, Cu, Ti, C, and O elements in the longitudinal direction (Figure 2b). Additionally, the original GF unit with excellent thermal conductivity has a high-crystalline structure, which is proved by the neglectable D peak (1350 cm^{-1}) in the Raman spectrum (Figure S9a, Supporting Information). The seamless bonding interfaces also exhibit polycrystalline textures with the (111) and (200) peaks of Ag and Cu in the XRD curves, which enhances the interlayer thermal conductivity of GTF compared with GTF-TAA (Figure S9b,c. Supporting Information).

Strong interfacial bonding is essential to ensure the structural stability and reliable thermal conductivity of GTF in long-term extreme environments. Considering the weak Van der Waals force in the graphene interlayers and impermeability between graphene and Cu,[50] a ternary interface with atomic Ti-assisted bonding is designed to enhance the strength of seamless bonding interfaces and also ensures low interfacial thermal resistance.[51,52] As shown in Figure 2c, MGF is seamlessly bonded together with a 5 mm overlapping length to conduct a lap-shear test.[43] The MGF with ternary bonding interface exhibits a strong joint strength of 180 kPa and a strain of 1%, which is higher than those of MGF without atomic Ti-assisted bonding (Figure 2d). Meanwhile, the interfacial peeling test also reveals the tighter bonding of MGF with the seamlessly ternary interface (Figure 2e).[53] It can be found that only the metal layer is taken away after peeling the MGF without atomic Ti bridging, leaving a relatively smooth GF surface. (Figure 2f; Figure S10, Supporting Information). In contrast, the peeling surface of MGF with ternary interfaces is rather rough and covered with graphene fragments. The density functional theory (DFT) theoretical calculations indicate that atomic Ti doping could boost the adhesion work of the graphene-Cu interfaces up to 0.62 J m^{-2}, 2.4 times higher than that of neat graphene-graphene interface (0.26 J m^{-2}), which originates from the intense interfacial charge transfer at the graphene/TiCu interface (Figure 2g,h; Figure S11, Supporting Information).[54] Furthermore, the MGF with ternary seamless interfaces maintains stable electrical conductivity even after 1000-times extreme bending from 0° to 180°, which also confirms the reliability of the ternary seamless interfaces (Figure S12, Supporting Information). This strong interfacial bonding lays the structural foundation to develop high-thermally conductive GTF in extreme environments.

2.3. Bidirectional Thermal Conductivity of GTF Over Wide Temperature Regions

Benefiting from the reliable seamless interface design for strong interface bonding of GTF-SBA, its thermal conductive properties are tested under different temperature ranges to meet future extreme thermal management (Figures S13 and S14, Supporting Information). At room temperature, the $\kappa_{\parallel}$ of GTF-SBA exhibits a moderating downward trend with the increase of thickness due to the more continuous and dense interfacial microstructures compared with GTF-TAA (**Figure 3a**). It is worth noting that the $\kappa_{\parallel}$ of GTF-SBA with extreme ≈250 µm thickness is 925.75 W m^{-1} K^{-1}, about twice the GTF-TAA (465.04 W m^{-1} K^{-1}. The electrical conductivity of GTF follows a similar trend to the in-plane thermal conductivity (Figure S15, Supporting Information). Moreover, the GTF-SBA demonstrates a record-breaking $\kappa_{\perp}$ of 7.5 W m^{-1} K^{-1} independent of thickness, which is ≈12.5 times GTF-TAA (0.6 W m^{-1} K^{-1}) (Figure 3b). The $\kappa_{\parallel}$ and thickness (h) are coupled with the heat flux of the GTF. The $\kappa_{\parallel}h$ of GTF-SBA (0.22 W K^{-1}) is 1.7 times that of the GTF-TAA (0.13 W K^{-1}) with ≈250 µm, which is beneficial to alleviating the high heat flux of high-power electronic devices (Figure 3c).

The alternating high and low temperatures in the aerospace industry pose new challenges to the structural stability of thermal management materials. Programmable extreme low-temperature shock tests are conducted from 77 to 298 K with liquid nitrogen. The $\kappa_{\parallel}$ of GTF-TAA sharply decreased by 70% after 200 cold impacts, whereas that of the GTF-SBA maintained stability (Figure 3d). This is because the seamless nanolayers of GTF-SBA effectively eliminate the interfacial pores and block the penetration of liquid nitrogen from surface defects to avoid catastrophic interlayer bubbling and separation (Figure S16, Supporting Information).[55] Simultaneously, the metallic seamless interfaces with low-temperature resistance and low thermal expansion coefficients also relieve the adhesion failure of traditional polymeric interfaces of GTF-TAA with brittleness breaking below the glass-transition temperature (Figure 3e; Figure S17, Supporting Information). The ultra-stability of GTF-SBA is also further supported by the fact that the XRD pattern and appearance of GTF-SBA remained nearly unchanged after multiple cold impacts (Figures S18 and S19, Supporting Information). In addition, the heat transport characteristics ($\kappa_{\parallel}$) of GTF-SBA are tested by an accurate steady-state method in the cryogenic zone, exhibiting a typical phonon-dominated low-temperature heat conduction with a 110 K transition point. Meanwhile, the $\kappa_{\parallel}$ of GTF-SBA could reach 1116.24 W m^{-1} K^{-1} even at 80 K, which is 2.0 times with pure Cu (561.01 W m^{-1} K^{-1}).[56] Therefore, the GTF-SBA assembled through seamless bonding could effectively improve the adaptability and thermal conductivity of graphene-based materials in extremely low-temperature environments, which is also beneficial for lightweight thermal management electronic devices in the scenarios of aerospace (Figure 3f).

Similarly, instantaneously extreme high-temperature environments also pose new challenges to the stable structures and performances of GTF. As shown in Figure 3g, the GTF-SBA possesses stable heat resistance at a wide temperature range from 323 to 773 K and the slight increase in mass after 523 K was due to the oxidation of a small amount of Ag, but the mass of GTF-TAA began to decline sharply at 473 K and lost 12% (Figure S20, Supporting Information). After 200 times heat impact from 298 to 573 K, the GTF-TAA suffers significant structural degradation because of the thermal decomposition of the polymeric adhesive, while the GTF-SBA remains in its original structure (Figure 3h). The $\kappa_{\parallel}$ of the GTF-TAA drastically decreases by almost 80% after thermal shocks, contrasted with the 95% retention of GTF-SBA (Figure 3i). This superior dimensional stability and thermal conductivity in the total temperature region demonstrate the reliable availability of the SBA strategy, allowing the use of GTF-SBA in future harsh conditions.

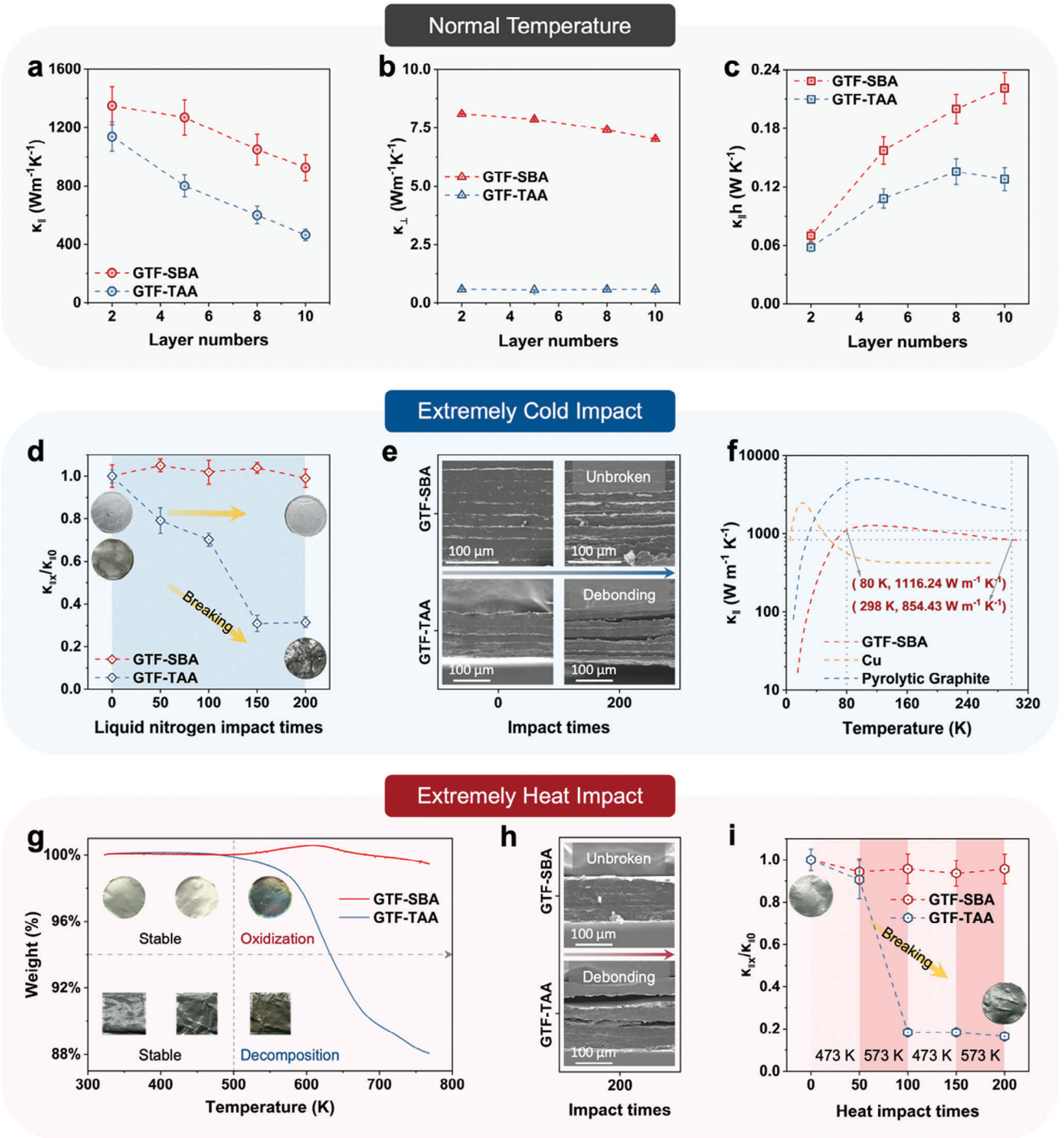

Figure 3. a) The in-plane thermal conductivity, b) through-plane thermal conductivity, and c) heat flow of GTF-TAA and GTF-SBA with different assembled layers, respectively. d) The variations of in-plane thermal conductivity of the GTF-TAA and GTF-SBA after different liquid nitrogen (77 K) impact times. e) Cross-sectional morphology of the GTF-TAA and GTF-SBA before and after 200 liquid nitrogen impacts. f) In-plane thermal conductivity of Cu, pyrolytic graphite, and GTF-SBA (50 layers) in the cryogenic zone. g) Thermogravimetric curve of GTF-TAA and GTF-SBA, insets show the surface morphology at different temperatures. h) Cross-sectional morphology of the GTF-TAA and GTF-SBA before and after 200 heat impacts. i) The variations of in-plane thermal conductivity of the GTF-TAA and GTF-SBA after different heat impact times.

2.4. Atomical Structures of Seamless Bonding Interfaces and their Effect on Thermal Conductivity

The ultra-stable microstructure and excellent bidirectional thermal conductive performances of GTF-SBA originated from the unique atomic structures of seamless bonding interfaces. We comprehensively investigated the microstructures of the seamless bonding interface and their effect on the thermal transport of the GTF-SBA. An atomic-scale model is illustrated to elucidate the hierarchical interfacial structures, including the modular GF unit, mutual diffusion layer, and ternary metal nanolayer (**Figure** 4a). There are two main seamless bonding interfaces in GTF-SBA, including the intermetallic Ag/Cu interfaces of ternary metal nanolayer and the ternary metal nanolayer/GF interfaces without apparent micro-voids (Figure 4b,c). The thickness of ternary metallic nanolayers is ≈478 nm, and relative elements are continuously and uniformly distributed around the GTF-SBA, which determines the stable bonding of GF units (Figure 4d,e). To reveal the atomic interfacial structure evolution of the seamless bonding interfaces, we conduct atomically resolved AC-STEM to observe the heterointerfaces. As shown in Figure 4f, there is an obvious penetration interface with ≈2 nm width of the metallic Ag/Cu nanolayer while in the bulk Ag and Cu nanolayers, they are polycrystalline texture, which is also proved by the corresponding SAED. These crystalline configurations of metal layers at the interfaces ensure the sealing of surface defects and serve as a permeability barrier of extreme liquid nitrogen. Focusing on the seamless bonding interfaces of GF unit and ternary metallic nanolayers, the continuous, dense, and amorphous diffusion interfaces are clearly formed due to the high-energy atom bombardment on the GF surface during magnetron sputtering, ensuring the strong covalence combination of metal and graphene (Figure 4g,i). Moreover, the bulk GF units still have a perfect layered graphene structure with 0.335 nm layer spacing, indicating a high crystallinity to guarantee the ultra-high $\kappa_{\parallel}$ of GTF-SBA (Figure 4h). It is found that there are some local lattice strains at the Cu/Ti/C interface and the Ag/Cu interface due to the atomic diffusion to also form atomic-scale solid mechanical interlocking structures (Figure 4j,k). The available mechanical interlocking effect of the GF/metal interface and effective covalent bonding of the Ti-C transition layer bond of the seamless bonding interfaces can both be attributed to realizing a strong adhesion of GTF-SBA and also increase the transport of phonon and electron in the graphene interlayer with the traditional van der Waals interactions, which is benefitted for the undesired $\kappa_{\perp}$ of previous GTF.[57–59] And the weak orientation and random entanglement of polymeric chains lead to serious phonon scattering, which cannot achieve rapid heat conduction of GTF-TAA. Therefore, the conformal design of seamless bonding interfaces effectively eliminates the interfacial porosity and greatly enhances the interlayer interaction to boost the structural integration and bidirectionally thermal conductivity.

2.5. Practical Applications and Thermal Conductivity Comparisons of GTF

Compared with other unidirectional thermal conductive film materials, the bidirectionally high-thermally conductive GTF-SBA can meet the efficient heat dissipation requirements of high-power electronic devices. Specifically, increasing the heat flux of GTF is basically conducive to realizing rapid heat dissipation of high-power electronic devices. The infrared image shows a faster and more uniform temperature distribution of GTF-SBA (≈250 μm) compared with a single MGF unit (26 μm), indicating a larger heat-transfer capacity of thick GTF-SBA (Figure S21, Supporting Information). To further compare the heat-transfer capability of GTF-TAA and GTF-SBA, the heat source is placed at the bottom of the samples and removed after a period with an in-situ temperature record (**Figure** 5a). The surface temperature of GTF-SBA rises faster during the heating process, which is 8.8 K higher than that of GTF-TAA, and drops faster during the cooling process (Figure 5b). Attributed to the bidirectional high thermal conductivity of GTF-SBA, superior thermal transport ($\kappa_{\perp}$) and desirable heat dissipation performance ($\kappa_{\parallel}$) are both achieved compared with GTF-TAA (Figure 5c). Notably, different from the existing reported GTF for thermal management, a gentler downward trend of $\kappa_{\parallel}$ with thickness and the highest $\kappa_{\perp}$ of GTF-SBA are simultaneously realized, which totally benefit from the ideal seamless interfacial structures (Figure 5d,e; Table S2, Supporting Information). The GTF-SBA has the highest $\kappa_{\perp}$ and moderate anisotropic intensity contrasted with other anisotropic thermal conductive material systems, including layered materials, composites, and polymers (Figure 5f; Table S3, Supporting Information). To further inhibit thermal conductivity attenuation with thickness and obtain bidirectionally high-thermally conductive graphene thick film, optimizing the assembly unit, interface design, and preparation process will be a potential and feasible solution in the future. Furthermore, the GTF-SBA adopts lightweight and high-thermally conductive GF as the assembly unit with a nanoscale seamless metallic bonding layer (478 nm), exhibiting a low density of 2.45 g cm^{-3}. The obtained GTF-SBA with 126 μm thickness features a specific thermal conductivity of 518 mW m^2 kg^{-1} K^{-1} surpassing various typical polymer, metal, and ceramic materials-based thermal conductive materials (Figure 5g; Table S4, Supporting Information).

3. Conclusion

We propose a reliably seamless bonding engineering to prepare GTF with bidirectionally high thermal conductivity and ultra-stable structures for extreme thermal management. The lower interfacial porosity and higher interfacial strength through transforming conventional physical adhesion into covalent bonding ensure the structural stability and thermal conductivity of GTF under various extreme conditions. The $\kappa_{\parallel}$ of GTF-SBA (h ≈ 250 μm) is ≈925.75 W m^{-1} K^{-1}, and the $\kappa_{\perp}$ is ≈7.03 W m^{-1} K^{-1}, which is hard to obtain directly by the traditional adhesive assembly. Furthermore, benefiting from seamless bonding interfaces, the microstructures and thermal conductive properties of GTF-SBA remained stable even after 200 cold or heat impacts from 77 to 573 K. This work gives an insightful concept of the seamless assembling of GTF through interface design and opens new possibilities for future applications of graphene-based materials with high performance in extreme thermal management applications.

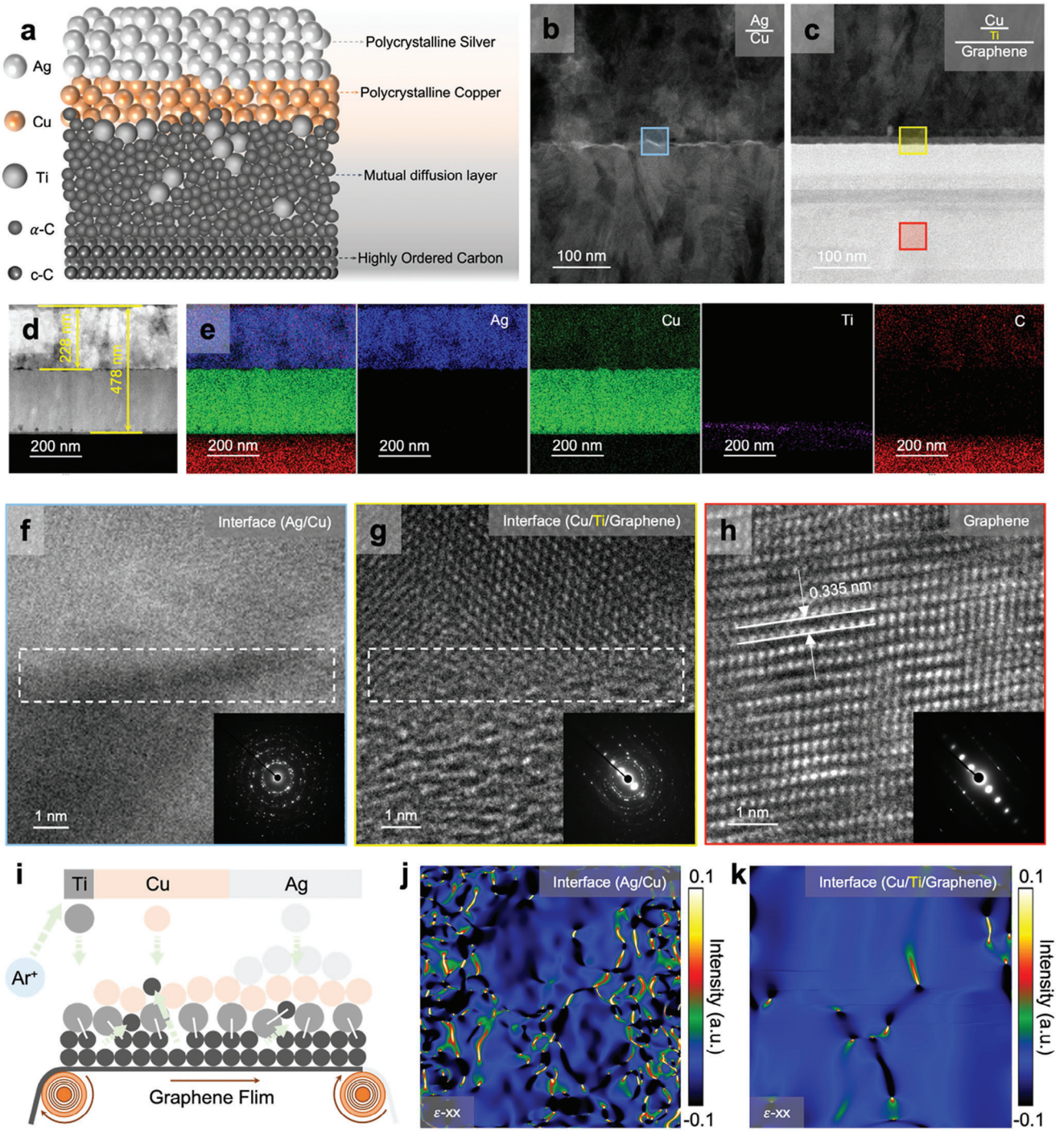

Figure 4. a) Schematic illustration of atomical seamless bonding interfaces of GTF-SBA. b,c) TEM images of the intermetallic (Ag/Cu) and ternary metal/graphene (Cu/Ti/Graphene) interfaces in the GTF-SBA. d) Correspondent thickness of ternary metal layers in the GTF-SBA. e) Elemental distribution of the seamless bonding interfaces of GTF-SBA. f–h) AC-STEM images of the intermetallic (Ag/Cu) and ternary metal/graphene (Cu/Ti/Graphene) interfaces and the high crystalline structures of GF unit of GTF-SBA, the insets are the corresponding SAED patterns. The seamless bonding interfaces are circled by white dotted lines. i) Illustration of the high-power atomic destruction process during the magnetron sputtering. j,k) Local lattice strain distribution of intermetallic (Ag/Cu) and ternary metal/graphene (Cu/Ti/Graphene) interfaces in the white box of Figure 4f,g by the GPA.

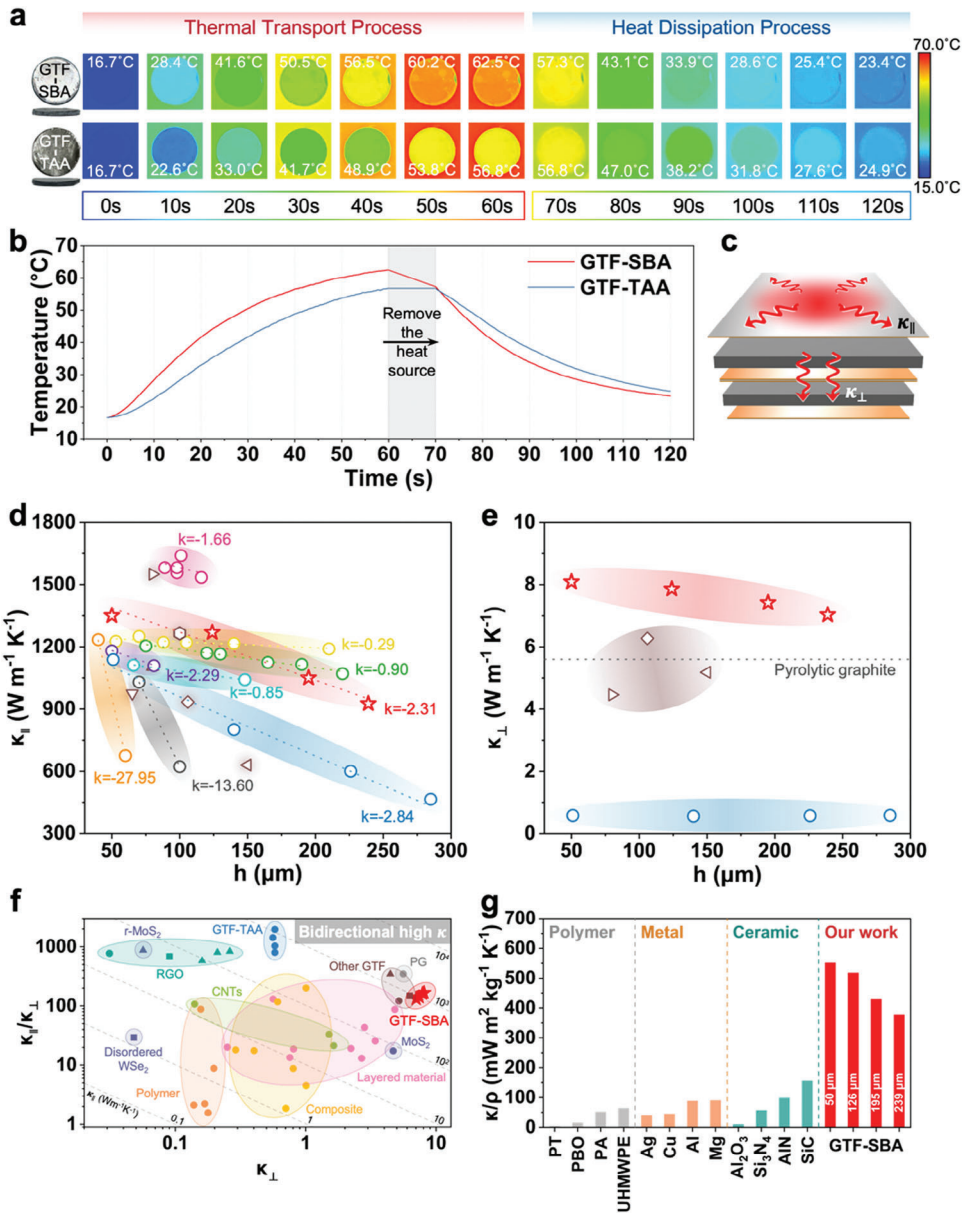

Figure 5. a) Infrared images, b) temperature distribution curves, c) and heat-transfer model of GTF-TAA and GTF-SBA with ≈1000 microns thicknesses under practical heat source heating and dissipation. d-e) Comparison of the in-plane and through-plane thermal conductivity of the GTF-SBA with GTF-TAA and reported GTF. f) Comparison of $\kappa_{\perp}$ (x-axis), $\kappa_{\parallel}/\kappa_{\perp}$ (y-axis), and $\kappa_{\parallel}$ (diagonal dashed lines) of GTF with other anisotropic thermal conductive materials. g) Comparison of the specific thermal conductivity of the GTF-SBA with GTF-TAA, polymer, metal, and ceramic-based thermal management materials.

4. Experimental Section

Material: The highly thermally conductive graphene films with 25 μm thickness were purchased from Gaoxi Technology Co., LTD. in Hangzhou, China. The traditional ultra-thin optical tapes with 5 μm made up of transparent PET substrate coated with acrylic adhesive were purchased from Zuanyi Electronics Co., LTD. in Suzhou, China.

Preparation of the GTF-TAA: The GF was cleaned in acetone and alcohol solution successively for 15 min, and then rinsed with deionized water and dried naturally to remove impurities introduced in the preparation process. Then multiple pieces of GF were mechanistically stuck layer-by-layer with double-side adhesive tape to obtain the graphene thick film from traditional adhesive assemble (GTF-TAA) with different thicknesses. Finally, the samples were cold-pressed (10 MPa, 12 h) to compact the whole closely. The samples were cut into circles ($\varnothing_1$ = 12.7 mm and $\varnothing_2$ = 25.4 mm) as required for the test.

Preparation of the GTF-SBA: The ion implantation technique was adapted to introduce trace reactive titanium (Ti) on the surface of the pristine GF. Subsequently, the Cu and Ag layers were sequentially deposited on both surfaces of the Ti-modified GF by magnetron sputtering. Considering the softening and fusion of metals during hot pressing, Ag, which was soft and had a lower melting point and high thermal conductivity, was more suitable as the outermost adhesive layer to weld multiple independent MGFs (Table S5, Supporting Information). Thereby, the metalized

graphene film (MGF) was prepared by ternary metal layer bonding. Similarly, the MGF was cut into circles ($\varnothing_1$ = 12.7 mm and $\varnothing_2$ = 25.4 mm). Multiple pieces of the MGF were filled into the graphite mold layer-by-layer and were welded through the spark plasma sintering (SPS) to obtain the graphene thick film from seamless bonding assemble (GTF-SBA) with different thicknesses. The SPS process was heated in a gradient manner and applied uniaxial pressure (10 MPa) under a high vacuum (less than 1×10^{-3} torr).

Other experimental details and any associated references are available in the Supporting Information.

Supporting Information

Supporting Information is available from the Wiley Online Library or from the author.

Acknowledgements

Y.H. and X.M. contributed equally to this work. This work is supported by the National Key Research and Development (R&D) Program of China (nos. 2022YFF0609801, 2022YFA1205300, 2022YFA1205301, and 2020YFF0204400), National Natural Science Foundation of China (Nos. 52272046, 52090030, 52090031, 52122301, and 51973191), the Natural Science Foundation of Zhejiang Province (LR23E020003), "Pioneer" and "Leading Goose" R&D Program of Zhejiang (2023C01190), Shanxi-Zheda Institute of New Materials and Chemical Engineering (2022SZ-TD011, 2022SZ-TD012, 2022SZ-TD014, and 2021SZ-FR004), Xinmiao Talents Program of Zhejiang Province (2023R401193), Hundred Talents Program of Zhejiang University (188020*194231701/113, 112300+1944223R3/003, and 112300+1944223R3/004), and the Fundamental Research Funds for the Central Universities (NOs. 226-2023-00023 and K20200060).

Conflict of Interest

The authors declare no conflict of interest.

Data Availability Statement

The data that support the findings of this study are available from the corresponding author upon reasonable request.

Keywords

extreme thermal management, graphene thick film, high thermal conductivity, seamless bonding assembly, structural stability

Received: January 3, 2024
Revised: February 25, 2024
Published online:

[1] A. Slippey, M. Ellis, B. Conway, H. C. Yun, in *SAE 2014 Aerospace Systems and Technology Conference*, SAE International, Warrendale, Pennsylvania **2014**.
[2] *Nat. Mater.* **2016**, *15*, 803.
[3] N. P. Padture, *Nat. Mater.* **2016**, *15*, 804.
[4] M. M. Waldrop, *Nature* **2016**, *530*, 144.
[5] N. Blet, S. Lips, V. Sartre, *Appl. Therm. Eng.* **2017**, *118*, 490.
[6] H. Song, J. Liu, B. Liu, J. Wu, H.-M. Cheng, F. Kang, *Joule* **2018**, *2*, 442.
[7] M. Cao, Z. Li, J. Lu, B. Wang, H. Lai, Z. Li, Y. Gao, X. Ming, S. Luo, L. Peng, Z. Xu, S. Liu, Y. Liu, C. Gao, *Adv. Mater.* **2023**, *35*, 2300077.
[8] C. Leng, X.-D. Wang, W.-M. Yan, T.-H. Wang, *Energy Convers. Manag.* **2016**, *110*, 154.
[9] W. Sun, Z. Han, X. Yue, H. Zhang, K. Yang, Z. Liu, D. Li, Y. Zhao, Z. Ling, H. Yang, Q. Guan, S. Yu, *Adv. Mater.* **2023**, *35*, 2300241.
[10] Q.-F. Guan, H.-B. Yang, Z.-M. Han, L.-C. Zhou, Y.-B. Zhu, Z.-C. Ling, H.-B. Jiang, P.-F. Wang, T. Ma, H.-A. Wu, S.-H. Yu, *Sci. Adv.* **2020**, *6*, eaaz1114.
[11] H. Lee, D. Lee, Y. Kim, *Energy Convers. Manag.* **2022**, *252*, 115092.
[12] M. Zeneli, A. Bellucci, G. Sabbatella, D. M. Trucchi, A. Nikolopoulos, N. Nikolopoulos, S. Karellas, E. Kakaras, *Energy Convers. Manag.* **2020**, *210*, 112717.
[13] R. C. Walker, A. E. Potochniak, A. P. Hyer, J. K. Ferri, *Adv. Colloid Interface Sci.* **2021**, *295*, 102464.
[14] Q. Chen, Z. Ma, Z. Wang, L. Liu, M. Zhu, W. Lei, P. Song, *Adv. Funct. Mater.* **2022**, *32*, 2110782.
[15] X. Zhao, W. Li, Y. Wang, H. Li, J. Wang, *Carbon* **2021**, *181*, 40.
[16] K. S. Novoselov, A. K. Geim, S. V. Morozov, D. Jiang, Y. Zhang, S. V. Dubonos, I. V. Grigorieva, A. A. Firsov, *Science* **2004**, *306*, 666.
[17] Z. Han, J. Wang, S. Liu, Q. Zhang, Y. Liu, Y. Tan, S. Luo, F. Guo, J. Ma, P. Li, X. Ming, C. Gao, Z. Xu, *Adv. Fiber Mater.* **2022**, *4*, 268.
[18] Y. Qi, Y. Xia, P. Li, Z. Wang, X. Ming, B. Wang, K. Shen, G. Cai, K. Li, Y. Gao, Y. Liu, C. Gao, Z. Xu, *Adv. Fiber Mater.* **2023**, *5*, 2016.
[19] K. S. Novoselov, A. Mishchenko, A. Carvalho, A. H. Castro Neto, *Science* **2016**, *353*, aac9439.
[20] Q. Wei, S. Pei, X. Qian, H. Liu, Z. Liu, W. Zhang, T. Zhou, Z. Zhang, X. Zhang, H. Cheng, W. Ren, *Adv. Mater.* **2020**, *32*, 1907411.
[21] X. Ming, A. Wei, Y. Liu, L. Peng, P. Li, J. Wang, S. Liu, W. Fang, Z. Wang, H. Peng, J. Lin, H. Huang, Z. Han, S. Luo, M. Cao, B. Wang, Z. Liu, F. Guo, Z. Xu, C. Gao, *Adv. Mater.* **2022**, *34*, 2201867.
[22] H. Peng, X. Ming, K. Pang, Y. Chen, J. Zhou, Z. Xu, Y. Liu, C. Gao, *Nano Res.* **2022**, *15*, 4902.
[23] S. Luo, L. Peng, Y. Xie, X. Cao, X. Wang, X. Liu, T. Chen, Z. Han, P. Fan, H. Sun, Y. Shen, F. Guo, Y. Xia, K. Li, X. Ming, C. Gao, *Nano-Micro Lett.* **2023**, *15*, 61.
[24] Q. Zhang, Q. Wei, K. Huang, Z. Liu, W. Ma, Z. Zhang, Y. Zhang, H.-M. Cheng, W. Ren, *Natl. Sci. Rev.* **2023**, *10*, nwad147.
[25] F. Wang, W. Fang, X. Ming, Y. Liu, Z. Xu, C. Gao, *Appl. Phys. Rev.* **2023**, *10*, 011311.
[26] H. Shi, B. Wang, L. Wang, P. Zhang, X. Ming, Y. Hao, J. Lu, Y. Gao, W. Gao, H. Sun, P. Li, Z. Xu, Y. Liu, C. Gao, *Carbon* **2024**, *221*, 118947.
[27] H. Ma, M. Fashandi, Z. B. Rejeb, X. Ming, Y. Liu, P. Gong, G. Li, C. B. Park, *Nano-Micro Lett.* **2024**, *16*, 20.
[28] S. Zhou, Y. Zhu, H. Du, B. Li, F. Kang, *New Carbon Mater.* **2012**, *27*, 241.
[29] D. A. Dikin, S. Stankovich, E. J. Zimney, R. D. Piner, G. H. B. Dommett, G. Evmenenko, S. T. Nguyen, R. S. Ruoff, *Nature* **2007**, *448*, 457.
[30] Z. Liu, Z. Li, Z. Xu, Z. Xia, X. Hu, L. Kou, L. Peng, Y. Wei, C. Gao, *Chem. Mater.* **2014**, *26*, 6786.
[31] J. Zhong, W. Sun, Q. Wei, X. Qian, H.-M. Cheng, W. Ren, *Nat. Commun.* **2018**, *9*, 3484.
[32] D. C. Price, *IEEE Trans. Comp. Packag. Technol.* **2003**, *26*, 26.
[33] Y. Kaburagi, T. Kimura, A. Yoshida, Y. Hishiyama, *Tanso* **2012**, *253*, 106.
[34] X. H. Wei, L. Liu, J. X. Zhang, J. L. Shi, Q. G. Guo, *J. Mater. Sci.* **2010**, *45*, 2449.
[35] G. Xin, H. Sun, T. Hu, H. R. Fard, X. Sun, N. Koratkar, T. Borca-Tasciuc, J. Lian, *Adv. Mater.* **2014**, *26*, 4521.
[36] J.-J. Shao, W. Lv, Q.-H. Yang, *Adv. Mater.* **2014**, *26*, 5586.
[37] X. Li, G. Zhang, X. Bai, X. Sun, X. Wang, E. Wang, H. Dai, *Nat. Nanotechnol.* **2008**, *3*, 538.
[38] Y. Zhang, H. Han, N. Wang, P. Zhang, Y. Fu, M. Murugesan, M. Edwards, K. Jeppson, S. Volz, J. Liu, *Adv. Funct. Mater.* **2015**, *25*, 4430.

[39] S. Wan, Y. Chen, S. Fang, S. Wang, Z. Xu, L. Jiang, R. H. Baughman, Q. Cheng, *Nat. Mater.* **2021**, *20*, 624.
[40] S. Wan, X. Li, Y. Chen, N. Liu, Y. Du, S. Dou, L. Jiang, Q. Cheng, *Science* **2021**, *374*, 96.
[41] S. Chen, Q. Wang, M. Zhang, R. Huang, Y. Huang, J. Tang, J. Liu, *Carbon* **2020**, *167*, 270.
[42] T. Wu, Y. Xu, H. Wang, Z. Sun, L. Zou, *Carbon* **2021**, *171*, 639.
[43] X. Zhang, Y. Guo, Y. Liu, Z. Li, W. Fang, L. Peng, J. Zhou, Z. Xu, C. Gao, *Carbon* **2020**, *167*, 249.
[44] S. Yang, Z. Tao, Q. Kong, J. Li, X. Li, X. Yan, J. Liu, Y. Tong, Z. Liu, *Chem. Eng. J.* **2023**, *473*, 145330.
[45] J. Lin, P. Li, Y. Liu, Z. Wang, Y. Wang, X. Ming, C. Gao, Z. Xu, *ACS Nano* **2021**, *15*, 4824.
[46] Y. Liu, P. Li, F. Wang, W. Fang, Z. Xu, W. Gao, C. Gao, *Carbon* **2019**, *155*, 462.
[47] N. Burger, A. Laachachi, M. Ferriol, M. Lutz, V. Toniazzo, D. Ruch, *Prog. Polym. Sci.* **2016**, *61*, 1.
[48] V. B. Mohan, K. Lau, D. Hui, D. Bhattacharyya, *Compos. Part B-Eng.* **2018**, *142*, 200.
[49] A. A. Balandin, *Nat. Mater.* **2011**, *10*, 569.
[50] S. C. Tjong, *Mater. Sci. Eng. R* **2013**, *74*, 281.
[51] L. X. Zhang, Q. Chang, Z. Sun, J. J. Zhang, J. L. Qi, J. C. Feng, *Carbon* **2019**, *154*, 375.
[52] G. Chang, F. Sun, J. Duan, Z. Che, X. Wang, J. Wang, M. J. Kim, H. Zhang, *Acta Mater.* **2018**, *160*, 235.
[53] Y. Jiang, S. Ji, J. Sun, J. Huang, Y. Li, G. Zou, T. Salim, C. Wang, W. Li, H. Jin, J. Xu, S. Wang, T. Lei, X. Yan, W. Y. X. Peh, S.-C. Yen, Z. Liu, M. Yu, H. Zhao, Z. Lu, G. Li, H. Gao, Z. Liu, Z. Bao, X. Chen, *Nature* **2023**, *614*, 456.
[54] H. Guo, Y. Qi, X. Li, *J. Appl. Phys.* **2010**, *107*, 033722.
[55] P. Zhang, Y. Hao, H. Shi, J. Lu, Y. Liu, X. Ming, Y. Wang, W. Fang, Y. Xia, Y. Chen, P. Li, Z. Wang, Q. Su, W. Lv, J. Zhou, Y. Zhang, H. Lai, W. Gao, Z. Xu, C. Gao, *Nano-Micro Lett.* **2024**, *16*, 58.
[56] R. L. Powell, H. M. Roder, W. M. Rogers, *J. Appl. Phys.* **1957**, *28*, 1282.
[57] J. Wang, Z. Wang, K. Yang, N. Chen, J. Ni, J. Song, Q. Li, F. Sun, Y. Liu, T. Fan, *Adv. Funct. Mater.* **2022**, *32*, 2206545.
[58] M. Yang, Y. Liu, T. Fan, D. Zhang, *Prog. Mater. Sci.* **2020**, *110*, 100652.
[59] Y. Liu, Y. Huang, X. Duan, *Nature* **2019**, *567*, 323.